

Asymmetric transmission and coherent perfect absorption in a periodic array of thermoacoustic cells

Come Olivier, Anis Maddi, Gaëlle Poignand, Guillaume Penelet

▶ **To cite this version:**

Come Olivier, Anis Maddi, Gaëlle Poignand, Guillaume Penelet. Asymmetric transmission and coherent perfect absorption in a periodic array of thermoacoustic cells. Journal of Applied Physics, 2022, 131 (24), pp.064012. ⟨10.1063/5.0089989⟩. ⟨hal-04395161⟩

HAL Id: hal-04395161

https://hal.science/hal-04395161v1

Submitted on 6 Oct 2025

HAL is a multi-disciplinary open access archive for the deposit and dissemination of scientific research documents, whether they are published or not. The documents may come from teaching and research institutions in France or abroad, or from public or private research centers.

L'archive ouverte pluridisciplinaire **HAL**, est destinée au dépôt et à la diffusion de documents scientifiques de niveau recherche, publiés ou non, émanant des établissements d'enseignement et de recherche français ou étrangers, des laboratoires publics ou privés.



Distributed under a Creative Commons CC BY 4.0 - Attribution - International License

Asymmetric Transmission and Coherent Perfect Absorption in a periodic array of thermoacoustic cells

Come Olivier,[a] Anis Maddi, Gaelle Poignand, and Guillaume Penelet
Laboratoire d'Acoustique de l'Université du Mans (LAUM), UMR 6613, Institut d'Acoustique - Graduate School (IA-GS), CNRS, Le Mans Université, France

This paper describes some exotic scattering properties of a one-dimensional network of thermoacoustic cells, and characterizes them experimentally. The considered two-port consists of a waveguide containing a periodic arrangement of porous materials subjected to temperature gradients and separated by empty sections. The interaction of an acoustic wave with the temperature gradients leads to an inherently nonreciprocal phenomenon known as the thermoacoustic effect. It is shown that this effect can be exploited for the design of systems with exotic acoustic scattering properties through two experimental demonstrations. The first example showcases a balanced asymmetric transmitter with transmission coefficients inverse of each other, yielding a nonreciprocity factor of 18 dB, without reflections. The second example shows a coherent perfect absorber, where maximum absorption is achieved for a wide range of temperature gradients by controlling the relative amplitudes and phasing of incoming waves.

I. INTRODUCTION

Nonreciprocal systems are a subject of intense research, as they provide new ways to control wave propagation and absorption. Breaking reciprocity is a key to one-way propagation, a necessary feature for the design of efficient acoustic isolators, one-way mirrors or nonreciprocal topological insulators[1]. In recent years, strategies to break reciprocity made use of nonlinearities[2,3] moving media[4–6], spatiotemporal modulation[7], nonlinear bianisotropy[8] or active control[9,10]. Recent reviews covering the subject can be found in Refs.[11,12].

The thermoacoustic effect is another way to break reciprocity. Due to the viscous and thermal coupling between an oscillating fluid and a porous medium submitted to a temperature gradient, this effect may lead either to the amplification or to the damping of an incident wave, depending on the sign of the temperature gradient. For an "in-depth" yet accessible explanation of the thermoacoustic effect, the reader is referred to Ref. 13, while Refs. 14 and 15 will provide recent reviews covering the various thermoacoustic machines developed in the last decades. The thermoacoustic effect is therefore an inherently nonreciprocal phenomenon. In recent years, only a few studies have taken advantage of this effect to obtain exotic systems such as a thermoacoustic diode[16] exhibiting a 16 dB power-transmission ratio thanks to a four-stages thermoacoustic unit, or a system achieving spontaneous $\mathcal{PT}$-symmetry breaking through the balance of thermoacoustic amplification and damping[17]. Periodic arrangements of thermoacoustic cores have also recently been shown to be a form of Willis material exhibiting non reciprocal and even couplings[18,19]. This description offers a different way to describe one-dimensional periodic thermoacoustic networks, and should ultimately provide access to new means of controlling waves.

In this mostly experimental work, we propose to explore further some of the possibilities offered by a periodic array of thermoacoustic cells to control wave propagation. The theoretical description of the acoustic propagation in such a system is provided in Sec. II, leading to the expression of its theoretical transmission and reflection coefficients. Section III is dedicated to presenting the experimental setup for the measurement of the scattering matrix of two ThermoAcoustic Networks (TAN), designed to demonstrate experimentally two exotic scattering phenomena observed at specific frequencies.

In Section IV, a first configuration is presented, exhibiting reflectionless asymmetric transmission. More precisely, a specific array of thermoacoustic cells is designed so that, at some specific frequency, the balance of thermoacoustic amplification/damping is achieved in such a way that the two-port is reflectionless but nonreciprocal, giving rise to transmission coefficients being inverse with each other. The experimental result show a nonreciprocity factor (ratio of transmission coefficients) of 18 dB with almost no reflection at a frequency of 57 Hz.

In Section V, a second configuration is presented in the form of a Coherent Perfect Absorber which keeps the nonreciprocal property inherent to the thermoacoustic coupling. Such a system does not let any wave out, when excited simultaneously from both ends with impinging waves of appropriate relative amplitude and phase, due to a combination of wave interference and absorption along the system[20,21]. Experimental results demonstrate over 99.8 % absorption for impinging waves of relative amplitudes from 1:1 to 25:1 at an almost constant frequency of 70 Hz for increasing temperature gradients applied on each cell.

II. THERMOACOUSTIC NETWORK DESCRIPTION

Figure 1(a) shows a representation of the elementary unit of a periodic network of thermoacoustic cells [shown in Fig. 1(c)]. It is composed of the usual elements con-

[a] Now at: Centre de Transfert de Technologies du Mans, CTTM, 2 rue Thalès de Milet, 72000 LE MANS.

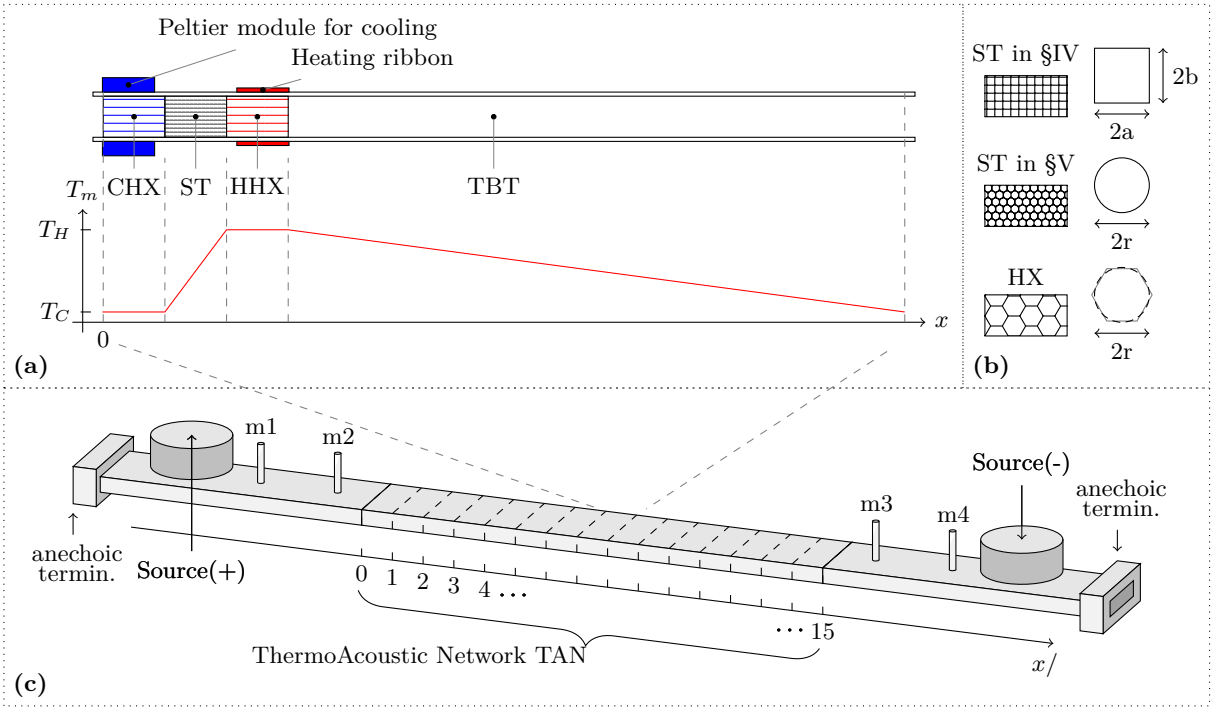


FIG. 1. (a) Unit cell of the ThermoAcoustic Network (TAN) showing the stack (ST) in which the thermoacoustic effect takes place, sandwiched between a hot heat exchanger and a cold heat exchanger (HHX and CHX resp. at temperatures T_H and T_C) imposing the temperature difference $\Delta T = T_H - T_C$ between its ends, and followed by a Thermal Buffer Tube (TBT) along which the temperature cycles back to T_C. (b) Pore geometries of both stacks (square pores for the asymmetric transmission in Sec.IV, circular pores for the coherent perfect absorber in Sec.V), and the heat exchangers (honeycomb modeled as circular pores) (c) Experimental setup for the measurement of the scattering matrix of the thermoacoustic network, showing the position of the anechoic terminations, the two sources providing the excitation signals and the four microphones (m1 to m4) required.

stituting a thermoacoustic core. The main element is a porous material where the thermoacoustic effect takes place, customarily called the stack[22] (denoted by ST). Two heat exchangers on either side allow a temperature gradient to be applied along the stack, from a cold temperature T_C to a hot temperature T_H. They are therefore referred to as the cold heat exchanger (CHX) and the hot heat exchanger (HHX), respectively. Lastly, the empty waveguide along which the temperature returns to T_C, is called the Thermal Buffer Tube (TBT). The TBT ensures the continuity of the temperature from cell to cell, such that the temperature field is identical in all cells.

Assuming a e^{iwt} temporal convention, the plane wave propagation through the four elements composing the unit cell is described by Rott's theory of linear thermoacoustics[23], such that the relation at position x between the acoustic pressure p and volume flow rate U oscillating at angular frequency ω is governed by

$$\begin{aligned}\frac{dp}{dx} &= -\frac{i\omega\rho_0}{S\phi(1-f_\nu)}U,\\ \frac{dU}{dx} &= -\frac{i\omega S\phi}{\gamma P_0}[1+(\gamma-1)f_\kappa]p\\ &\quad + \frac{f_\kappa - f_\nu}{(1-f_\nu)(1-\sigma)}\frac{1}{T_0}\frac{dT_0}{dx}U,\end{aligned} \tag{1}$$

where ρ_0 and P_0 represent the mean values of the density and the pressure of the fluid (air at atmospheric pressure in this case) and $\sigma = \nu/\kappa$ its Prandtl number, i.e. the ratio of its kinematic viscosity ν to its thermal diffusivity κ. These quantities depend implicitly on the mean temperature $T_0(x)$, and therefore are position-dependent. γ denotes the fluid's specific heat ratio. $S\phi$ is the open cross-section area available for the acoustic propagation, with ϕ the porosity of the constituents of the cell. Considering $\phi = 1$ allows to use Eq.(1) for empty waveguides (i.e. the TBT), whereas $\phi < 1$ in the heat exchangers and the stack.

$f_{\nu,\kappa}$ are frequency- and geometry-dependent functions that describe the viscous and thermal coupling between the oscillating gas and the surrounding solid walls[22,24]. They depend directly on the ratio of the characteristic dimension r of the channel to the viscous and thermal acoustic boundary layer thicknesses $\delta_{\nu,\kappa}$ given as $\delta_\nu = \sqrt{2\nu/\omega}$ and $\delta_\kappa = \sqrt{2\kappa/\omega} = \delta_\nu/\sqrt{\sigma}$. The expression of these functions varies with the geometry of the channel considered[25], see Fig. 1(b). For cylindrical channels of radius r, they are given as

$$f_{\nu,\kappa} = \frac{2}{(i-1)r/\delta_{\nu,\kappa}}\frac{J_1[(i-1)r/\delta_{\nu,\kappa}]}{J_0[(i-1)r/\delta_{\nu,\kappa}]} \tag{2}$$

where J_n is the nth order Bessel function of the first

kind. For rectangle channels of dimension $2a \times 2b$, their expression is given as the series

$$\begin{aligned} f_{\nu,\kappa} &= 1 - \left(\frac{8}{\pi^2}\right)^2 \sum_m \sum_n F_{m,n}^{\nu,\kappa}, \\ \frac{1}{F_{m,n}^{\nu,\kappa}} &= m^2 n^2 \left[1 - i\frac{\pi^2}{2}\left(\frac{\delta_{\nu,\kappa}}{r}\right)^2 \frac{b^2m^2 + a^2n^2}{(a+b)^2}\right] \end{aligned} \tag{3}$$

where $m, n = 1, 3, 5, \ldots$ and with the equivalent radius $r = 2ab/(a+b)$.

Note that an empty waveguide (i.e., the Thermal Buffer Tube) is described as a single large pore, with its characteristic dimension that of the waveguide.

Equations (1) can be used to express the transfer matrix $\mathbf{M}$ relating the pressure p and flow rate velocity U between two positions x_1 and x_2[22,26], such that:

$$\begin{pmatrix} p(x_2) \\ U(x_2) \end{pmatrix} = \mathbf{M} \begin{pmatrix} p(x_1) \\ U(x_1) \end{pmatrix} = \begin{bmatrix} M_{11} M_{12} \\ M_{21} M_{22} \end{bmatrix} \begin{pmatrix} p(x_1) \\ U(x_1) \end{pmatrix}. \tag{4}$$

It is worth noting that when the temperature is constant $dT_0/dx = 0$ (as is the case in the heat exchangers HX), Eqs. (1) fall back to the regular case of lossy propagation, yielding the transfer matrix over the length $d = x_2 - x_1$:

$$\mathbf{M}(\Delta T = 0) = \begin{bmatrix} \cos(kd) & -iZ_c \sin(kd) \\ \dfrac{-i}{Z_c} \sin(kd) & \cos(kd) \end{bmatrix}, \tag{5}$$

with $Z_c = \rho_0 c_0 / S\phi \left[(1-f_\nu)(1+(\gamma-1)f_\kappa)\right]^{-1/2}$ the lossy characteristic impedance of the waveguide and $k = \omega/c_0 \left[(1+(\gamma-1)f_\kappa)/(1-f_\nu)\right]^{1/2}$ the wavenumber, where c_0 is the adiabatic speed of sound.

The global transfer matrix $\mathbf{T}$ relating pressure and volume velocity at either end of a network composed of N_{cell} identical cells is obtained by multiplying sequentially the transfer matrices of each constitutive element, such that

$$\mathbf{T} = \left(\mathbf{M}_{\mathrm{TBT}} \mathbf{M}_{\mathrm{HHX}} \mathbf{M}_{\mathrm{ST}} \mathbf{M}_{\mathrm{CHX}}\right)^{N_{cell}}. \tag{6}$$

Incidentally, the acoustic pressure and volume velocity in the system can also be expressed as functions of the two counter-propagating pressure waves $p^\pm$, such that $p^+ = (Z_c p + U)/2$ and $p^- = (Z_c p - U)/2$. Therefore, the scattering matrix $\mathbf{S}$, describing the relation between the incoming $(p^-(x_2); p^+(x_1))$ and the outcoming $(p^-(x_1); p^+(x_2))$ acoustic waves on either sides of an element, can be deduced from Eq.(4) and is given by

$$\begin{pmatrix} p^-(x_1) \\ p^+(x_2) \end{pmatrix} = \mathbf{S} \begin{pmatrix} p^-(x_2) \\ p^+(x_1) \end{pmatrix} = \begin{bmatrix} t^- & r^+ \\ r^- & t^+ \end{bmatrix} \begin{pmatrix} p^-(x_2) \\ p^+(x_1) \end{pmatrix}. \tag{7}$$

wherein the transmission coefficients $t^\pm$ and the reflection coefficients $r^\pm$ are related to the transfer matrix coefficients T_{ij}, $(ij) \in [1,2]$ through the relations

$$\begin{aligned} t^- &= 2/\Omega, \\ r^+ &= (-T_{11} - T_{12}/Z_c + Z_c T_{21} + T_{22})/\Omega, \\ r^- &= (T_{11} - T_{12}/Z_c + Z_c T_{21} - T_{22})/\Omega, \\ t^+ &= 2(T_{11}T_{22} - T_{12}T_{21})/\Omega, \end{aligned} \tag{8}$$

with $\Omega = T_{11} - T_{12}/Z_c - Z_c T_{21} + T_{22}$.

With these theoretical tools now established for the description of the scattering properties of a 1-dimensional network of thermoacoustic cells, the following focuses on the presentation of the setup used to characterize the experimental scattering properties of networks designed with these tools.

III. EXPERIMENTAL SETUP

The experimental setup for the measurement of the scattering properties of a network of thermoacoustic cells is presented in Fig. 1(c). The central section is the scatterer to characterize, that consists of a periodic network of identical thermoacoustic cells. On either side of the network, two identical measurement sections allow for the measurement of its scattering coefficients.

A. Description of the TAN

The thermoacoustic network consists of a waveguide of rectangular $2a \times 2b = 1\,\mathrm{cm} \times 5\,\mathrm{cm}$ cross-section containing a regular layout of 15 identical thermoacoustic cells. Each cell is 19.5 cm long, resulting in a nearly 3 m long two-port. Each cell, as represented in Fig. 1(a), contains a stack, sandwiched between a cold and a hot heat exchanger controlling the temperature difference $\Delta T = T_H - T_C$ applied along the stack.

The stack is a porous material, characterized by its porosity ϕ and the radius of its pores r. In the following, two different materials are used to demonstrate two different kinds of scatterers, see Fig. 1(c). For the purpose of demonstration of an asymmetric transmitter in Section IV, the 15 mm long stack is carved out of cordierite catalytic substrate, consisting of many parallel square channels of equivalent radius $r = 585\,\mu\mathrm{m}$ (corresponding to 400 cells per square inch), with a porosity of $\phi = 0.85$. For the demonstration of a coherent perfect absorber in Section V, the 14 mm long stack is made of a pile of 60 fine stainless wire meshes (mesh number 45 and wire diameter 160 µm, ref.104738, Gantois Industries). Though irregular in shape, the pores of such a material can satisfactorily be modeled as of circular cross section. A fit of experimental data gives an evaluation of the average pore radius $r \approx 170\,\mu\mathrm{m}$ and a porosity $\phi \approx 0.80$.

The heat exchangers are used to ensure a uniform temperature distribution over the rectangular $1\,\mathrm{cm} \times 5\,\mathrm{cm}$ cross-section of the waveguide on each side of the stack. They are made of slices of 1/8" aluminium honeycomb. Here too, the hexagonal pores are modeled as circular, fitted from measurements to a pore radius $r \approx 770\,\mu\mathrm{m}$ and a porosity $\phi \approx 0.945$. The hot temperature is imposed to the hot heat exchangers through the 1 mm-thick stainless steel walls of the waveguide by 10 W polyimide heaters (KHLVA-0502/10-P, Omega Engineering) applied on each face of the waveguide, supplied by

Element	pore shape	pore size	porosity	length
ST (§IV)	square	585 µm	0.85	15 mm
ST (§V)	mehsgrids	170 µm	0.80	14 mm
HX	honeycomb	770 µm	0.945	15 mm
TBT	rectangular	1×5 cm	1	150 mm

TABLE I. Dimensions of the different elements of the thermoacoustic cell. Dimensions for the stack are given both for Reflectionless Asymmetric Transmission and Coherent Perfect Absorber configurations.

controlled DC power supplies (EA-PS 3065-10B, ElektroAutomatik). The cold temperature is imposed on the cold heat exchangers through the 1 mm-thick stainless steel walls of the waveguide, thanks to two 10.4 W Peltier cooler modules (ET-063-08-15, Adaptive, European Thermodynamics) on each side of the waveguide, supplied by a controlled DC power supply (CPX200DP, Aim-TTi Instruments). Water circulating in aluminum tubing in direct contact with their hot side evacuates the heat extracted by the Peltier modules.

A representation of the geometry of the pores of the different porous media (stacks and heat exhangers) used for this study is provided in Fig. 1(b).

Finally, the empty 15 cm TBT separates the hot heat exchanger from the cold heat exchanger of the following cell, limiting the amount of direct thermal leakage between cold and hot sources. The resulting temperature distribution is considered one-dimensional in the unit cell, homogeneous in the heat exchangers and varying linearly in the stack and the TBT, as is depicted in Fig. 1(a). Geometrical properties of the thermoacoustic unit cell are summarized in Table I.

B. Measurement setup

For the need of the measurement of the scattering matrix by means of the two-sources, four-microphones method[27], this thermoacoustic network is itself connected to another section of waveguide at each side. As illustrated in Fig. 1(c), each of these measurement sections consists of a straight 1.2 m waveguide with the same cross-section, on which a pair of 1/4" microphones (Brüel & Kjær 4136 with Nexus amplifier 2690) are flush mounted. Each microphone pair is separated by a distance of 65 cm, allowing measurement in the 10 Hz to 220 Hz range provided that they have been precisely calibrated (both in amplitude and phase) to limit the errors on the measured and calculated quantities[28]. A preliminary relative calibration has therefore been made using a small cavity coupler.

A moving coil loudspeaker (Visaton FRS 8) is side mounted near the end of the measurement section to provide the step-by-step harmonic excitation. The speaker is placed in a small enclosure and coupled to the waveguide via a a tube of centimetric diameter. The measurements are conducted with low enough excitation amplitudes that nonlinear effects of propagation can be discarded.

Each measurement section ends with a low frequency anechoic termination. Such a termination consists of a larger cavity (1.5 cm × 7 cm) with an adjustable length closed by stainless wire mesh screens[29,30]. The reflection coefficient of such terminations has a measured amplitude lower than 4 % over the frequency range of interest, which is a sufficiently low value for the needs of this study.

IV. REFLECTIONLESS BALANCED ASYMMETRIC TRANSMISSION

A first setup of the thermoacoustic network is sought to demonstrate reflectionless balanced asymmetric transmission. That is, we search a geometrical configuration of the network and properties of the stack configuration for which, at a given frequency f_1 and a temperature difference ΔT_1, its transmission coefficients are inverse of each other (and obviously non-unity) and the reflection coefficients are close to zero. The targeted properties of $\mathbf{S}$ can be summarized as

$$(|S_{ij}(f_1, \Delta T_1)|) = \begin{bmatrix} |t^-| & \sim 0 \\ \sim 0 & |t^+| = 1/|t^-| \end{bmatrix}. \qquad (9)$$

The chosen experimental configuration is built around 15 mm long cordierite substrate stacks with square pores of half width $r = 585\,\mu$m and porosity $\phi = 0.85$, offering the best theoretical results within the experimental constraints.

A. Theoretical results

The amplitude of the theoretical scattering coefficients of the system are shown with lines in Fig. 2(a-b) for increasing temperature differences ΔT =0 K, 50 K, 82 K and 106 K (from blue to yellow), evaluated for frequencies from 10 Hz to 250 Hz. The phase of the coefficients (not represented here) behaves as one would expect (i.e. the phase of the transmission coefficients is almost a linear function of frequency, that reflects the propagation of the wave through the two-port with a speed close to the adiabatic speed of sound.)

For $\Delta T = 0$ (blue curves), the system behaves as expected for a passive reciprocal and (almost) symmetric system, with transmission coefficients identical in both directions: both continuous and dashed blue lines are indistinguishable. Their amplitudes are less than unity $|t^{\pm}(\Delta T = 0)| < 1$ due to the propagation losses, mainly in the porous material constituting the stack and to a lesser extent in the heat exchangers. The reflection coefficients are also identical with magnitude $0 < |r^{\pm}| < 1$ (identical blue lines in Fig. 2). The variations of the reflection coefficients with the frequency are indicative of a Fabry-Perot-like interference behavior of the wave in

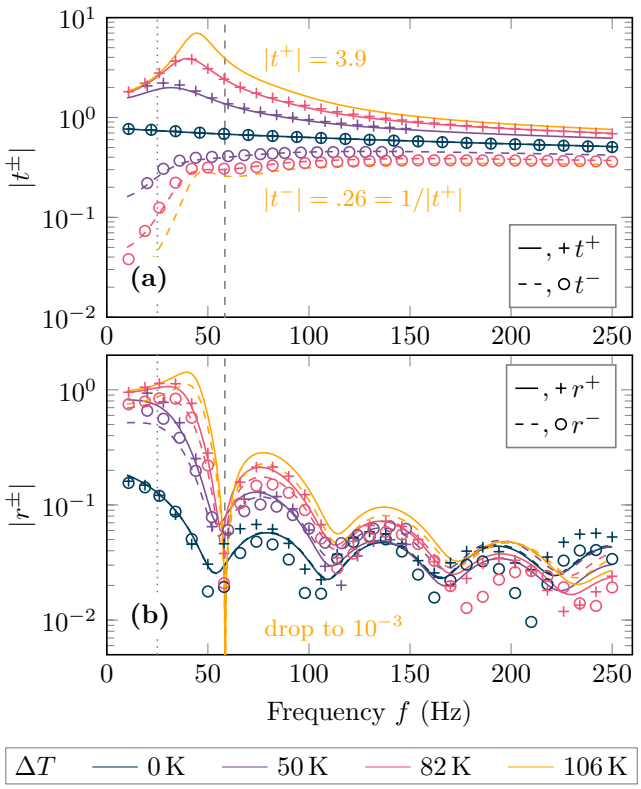


FIG. 2. Moduli of the (a) transmission coefficients and (b) reflection coefficients of the scattering matrix $\mathbf{S}$ of the 15 cells thermoacoustic network for various temperature differences $\Delta T = 0\,\mathrm{K}$, $50\,\mathrm{K}$, $82\,\mathrm{K}$ and $106\,\mathrm{K}$ (from blue to yellow, lines represent the model and markers show the measurement data points). Reflectionless asymmetric transmission is expected to happen for $\Delta T_1 = 106\,\mathrm{K}$ (yellow curves) at $f_1 = 57\,\mathrm{Hz}$ (marked by the vertical dashed line) with $|t^-| = 1/|t^+|$ and $|r^{\pm}| \ll 1$. This last temperature difference was not achievable experimentally.

the system, with $r^{\pm}$ dropping at a frequency related to the total length of the network $f_L \approx 2c_0/L$ and its multiples. Note that, the system being composed of highly porous materials, the transmission coefficients are larger than the reflection coefficients in the absence of heating.

For increasing temperature differences $\Delta T > 0$, both properties of reciprocity and symmetry of the network are lost. The transmission coefficients of the system are not identical anymore, highlighting a direction of propagation where the wave is amplified (in the direction of the positive temperature gradient in the stack) shown with continuous lines. In the opposite direction, the transmitted wave are attenuated, more strongly for higher temperature differences on the considered frequency range, as shown with dashed lines in Fig. 2(a). The behavior of the reflection coefficients, though slightly different in both directions, remains mainly driven by the interference of the waves with the periodic structure of the system in Fabry-Perot-like resonances. Note that, with the increase of the temperature gradient, the amplitude of the reflection coefficients becomes larger, especially at lower frequencies where they can become greater than unity.

For a temperature difference of $\Delta T_1 = 106\,\mathrm{K}$ (shown in yellow), the system is expected to behave as a reflectionless asymmetric transmitter at the frequency $f_1 = 57\,\mathrm{Hz}$. Its reflection coefficients should drop considerably (see Fig. 2(b)), while its transmission coefficients should be inverse of each other $|t^-| = 0.26 = 1/|t^+|$ with $|t^+| = 3.9$, as pointed in Fig. 2(a).

B. Experimental results

Experimental data points corresponding to the modeled conditions are presented with markers in Fig. 2, respectively crosses for the coefficients t^+ and r^+, and circles for t^- and r^-.

In the absence of a temperature gradient, measurements confirm the reciprocity of the network, with the superposition of the blue crosses and circles. With increasing temperature differences, the scattering coefficients follow the predicted behavior. The transmission coefficients are in very good agreement with the model. The reflection coefficients, though slightly carrying the perturbation observed at $\Delta T = 0$, still follow closely the modeled evolution, with $|r^+|$ being larger than $|r^-|$.

The predicted temperature difference of $\Delta T_1 = 106\,\mathrm{K}$ proved to be not reachable with the experimental setup due to heat input limitations. However, the data set corresponding to the highest experimental temperature difference $\Delta T = 82\,\mathrm{K}$ (pink) is already worth of interest. At the frequency of interest, namely $\sim 57\,\mathrm{Hz}$, the experimental coefficients of reflection experience a minimum, with respectively $|r^+| \approx 0.04$ and $|r^-| \approx 0.02$, while the transmission coefficients are not far to balance with $|t^+| \approx 2.5$ and $|t^-| \approx 1/3.2$. These results show a nonreciprocity factor (defined as the ratio of both transmission coefficients) of 18 dB.

To further illustrate the operation of the reflectionless balanced asymmetric transmitter, the propagation of monochromatic waves is studied, in conditions corresponding to $\Delta T = 82\,\mathrm{K}$ (pink markers) and at two frequencies, with different scattering properties. Figure 3 shows temporal measurements of waves propagating through the network from either direction and at the two frequencies indicated by the vertical lines in Fig. 2. The first frequency $f = 57\,\mathrm{Hz}$ corresponds to the drop of the reflection coefficients. It is representative of the target result, though exact balance was not totally achieved between the opposite directions of propagation. The second frequency $f = 25\,\mathrm{Hz}$ depicts the typical behavior of the scatterer at other frequencies, where the asymmetric transmission is perturbed by the strong reflection coefficients on both ends of the system.

In the case of $f = 57\,\mathrm{Hz}$ (indicated by the dashed line in Fig. 2), the experimental coefficients of reflection are small, respectively $|r^+| \approx 0.04$ and $|r^-| \approx 0.02$.

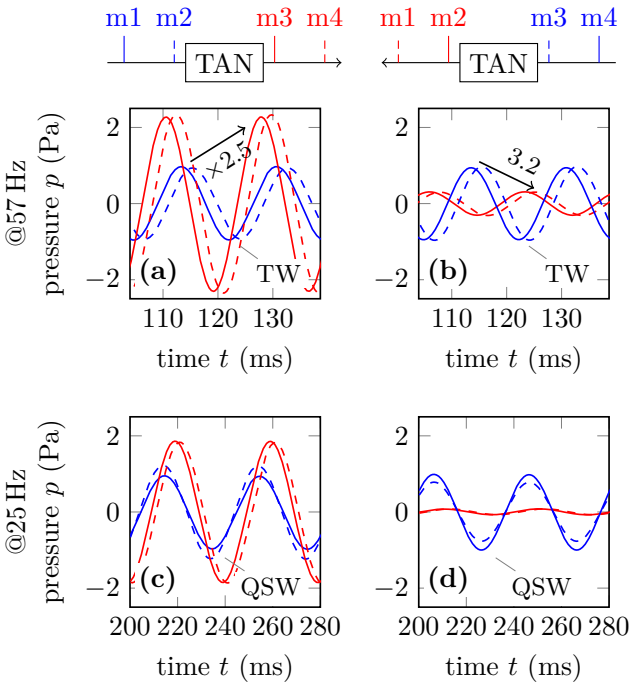


FIG. 3. Measured propagation of a continuous signals of unitary peak amplitude at 57 Hz and 25 Hz with $\Delta T = 82$ K by the four microphones in the setup, excited either from the left or from the right. Blue lines show upstream waves, and red lines downstream waves. The top sequences (a-b) are for 57 Hz that corresponds to the drop of the reflection coefficients, with the transmissions such that $|t^+t^-| \sim 1$, marked by the vertical dashed line in Fig. 2. Both upstream and downstream signal pairs are phased with a delay corresponding to the propagation of a traveling wave (TW) along the distance separating the microphones in either direction. The bottom sequences (c-d) at 25 Hz correspond to the dotted line in Fig. 2, with a strong attenuation in the $(-x)$-direction coupled with near unity reflections in both directions, inducing upstream quasi-standing waves (QSW) as demonstrated by the blue signals in phase.

As a consequence, the measured upstream waves are quasi-traveling, as is demonstrated by the blue curves in Fig. 3(a-b), both having the same amplitude but being delayed by the time of flight between the microphones. Thanks to the anechoic terminations, the transmitted waves (in red, continuous then dashed lines) are purely traveling, and therefore measured by the two downstream microphones with a constant amplitude and a phase difference corresponding to the time of flight separating the measurement points. In this case, the amplitudes of the downstream waves are direct translation of the transmission coefficients: the wave propagating in the $(+x)$-direction is amplified by a factor of 2.5, whereas the wave propagating in the opposite direction is attenuated with a factor of $3.2:1$.

In the case of $f = 25$ Hz indicated by the vertical dotted line in Fig. 2, the individual coefficients of $\mathbf{S}$ do not fulfill the target requirements of Eq.(9): both reflections coefficients are indeed close to unity. As a consequence on corresponding temporal measurements (Fig. 3.c-d), the upstream waves (shown in blue) appear as quasi-standing waves, the signals measured at different distances of the network being almost in phase. Without knowledge of the amplitude of the impinging waves, further interpretation of the temporal signals in this case is rendered more difficult.

V. COHERENT PERFECT ABSORPTION

A second setup of the thermoacoustic network is sought to demonstrate coherent perfect absorption. That is, we search a geometrical configuration of the network and properties of the stack configuration for which, at a given frequency f_2 and a temperature difference ΔT_2, the output of the network is null. This translates in one of the eigenvalues λ_{min} of its transfer matrix $\mathbf{S}$ going through a minimum, with the lowest value possible. If this conditions are met, by exciting the network simultaneously from both ends with continuous signals at the frequency f_2 with relative amplitudes and phase difference given by the corresponding eigenvector q_{min}, the output waves should be of correspondingly small amplitudes. The target properties for the system may be summarized[31] as

$$\mathbf{S}(f_2) = \mathbf{Q} \begin{bmatrix} \lambda_{max} & 0 \\ 0 & \lambda_{min} \sim 0 \end{bmatrix} \mathbf{Q}^{-1}. \qquad (10)$$

where $\mathbf{Q}$ is the square matrix whose nth column is the eigenvector q_n of $\mathbf{S}$.

A. Theoretical results

Such a behavior is predicted to be achievable with the same thermoacoustic network by replacing the ceramic stack with a 14 mm stack with pores of radius $r_{th} \sim 160\,\mu$m, and porosity $\phi = 0.8$. Such dimensions are achieved by stacking 60 fine stainless wire meshes (mesh number 45 and wire diameter 160 µm, ref.104738, Gantois Industries). The properties of the stack fitted to emulate its experimental characterization are set to a porosity $\phi = 0.8$ and a pore radius $r_{exp} = 170\,\mu$m.

Fig. 4(a) shows the expected moduli of the eigenvalues of the scattering matrix of the 15-cells system for increasing temperature difference on each cell varying from $\Delta T = 0$ K to 75 K with increments of 15 K (blue to yellow). One of the eigenvalues, represented with continuous lines, shows a minimum around 70 Hz for temperature differences up to 75 K. A zoom on these minima (marked by the triangles on Fig. 4(b)) shows a nearly constant small amplitude of the eigenvalue around $3 \cdot 10^{-2}$. This eigenvalue is hereafter designated as λ_{min}. The other eigenvalue λ_{max} is shown with dashed lines. It is worth noting that the acoustic lasing effect expected to take place at the same frequency in a symmetrical system and

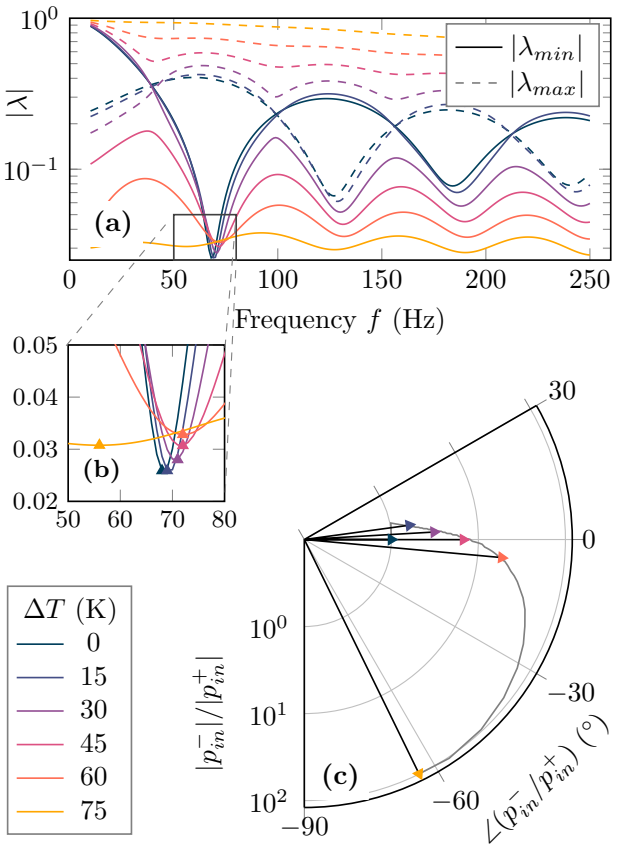


FIG. 4. (a) Theoretical amplitudes of the eigenvalues $|\lambda|$ of the scattering matrix $\mathbf{S}$ of the 15-cells thermoacoustic network as functions of the frequency and for increasing temperature difference $\Delta T = 0\,\mathrm{K}$ to $75\,\mathrm{K}$ in $15\,\mathrm{K}$ increments (blue to yellow). The eigenvalue showing a drop for a frequency of $f_2 \sim 70\,\mathrm{Hz}$ will be called λ_{min} and is shown by a continuous line. (b) Relative magnitude of the input pressure waves $|p_{in}^-|/|p_{in}^+|$ versus their phase difference $\varphi = \angle(p_{in}^-/p_{in}^+)$ at the points shown in the zoomed insert. The trajectory followed versus ΔT is traced in gray to ease reading: from $\Delta T = 0\,\mathrm{K}$ to $75\,\mathrm{K}$, the amplitude ratio change from $1:1$ to a $100:1$ while the phase shifts from in phase to $-60°$.

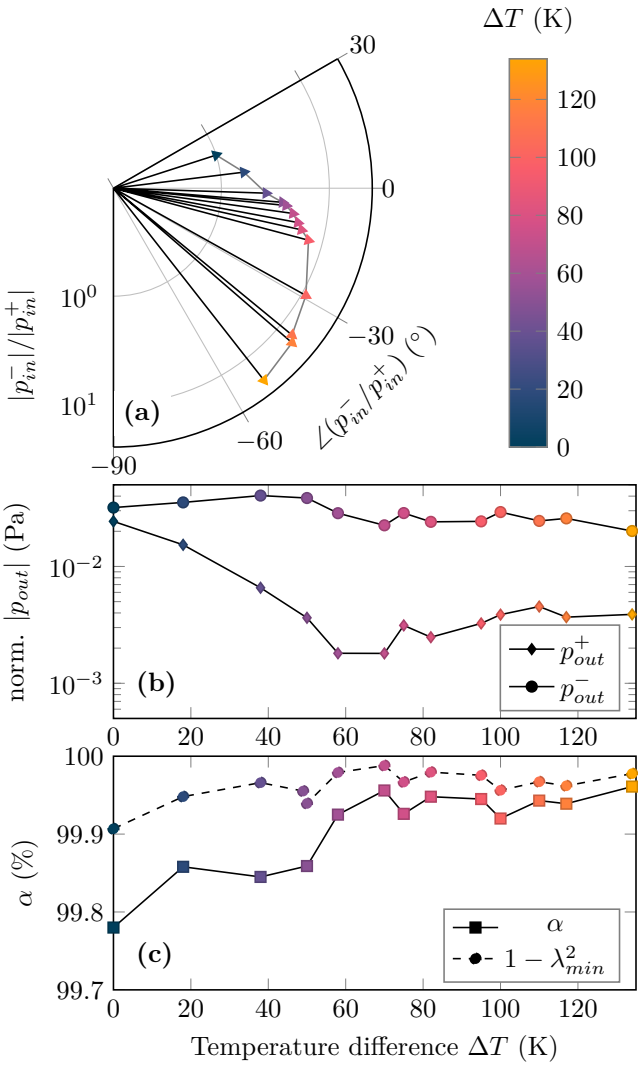


FIG. 5. (a) Amplitude ratio and phase of the input pressure waves as functions of the temperature difference ΔT measured on the outer wall of the system, in the range $0\,\mathrm{K}$ to $134\,\mathrm{K}$ (blue to red). (b) Magnitude of the outcoming pressure waves (normalized such that $|p_{in}^+|^2 + |p_{in}^-|^2 = 1\,\mathrm{Pa}^2$). (c) Resulting measured absorption coefficient α of the thermoacoustic network.

translating in λ_{max} peaking is not observed here (opposite to what is shown in[32,33]). This absence is due to the asymmetry in construction of the unit cell in addition to being nonreciprocal.

For each of the eigenvalues λ_{min}, the corresponding eigenvector is evaluated and shown in the polar plot (Fig. 4(c)). It is represented as the relative amplitudes of the incident waves $|p_{in}^-|/|p_{in}^+|$ versus their phase difference $\varphi = \angle(p_{in}^-/p_{in}^+)$ yielding the minimal output from the network, for each temperature difference. The acoustic input condition required to reach the coherent perfect absorption shows an important shift of amplitude ratio, which changes from $1:1$ to a $100:1$ while the phase shifts from in phase to $-60°$ over the studied temperature difference range. The trajectory followed by the eigenvector is shown with a gray line to help with readability.

B. Experimental results

The scattering matrix $\mathbf{S}$ of the two-port is measured for several conditions of heating. From the measurement of $\mathbf{S}$, the eigenvalues and associated eigenvectors are computed. Focusing on the frequency of interest (in the range $65\,\mathrm{Hz} < f_{2,\mathrm{exp}} < 70\,\mathrm{Hz}$ changing slowly with ΔT), the relevant eigenvalue reaching a minimum, is selected with its associated eigenvectors.

In Figure 5(a), the relative amplitudes and phase differences of the eigenvectors producing the minima of

λ_{min} are reported for increasing temperature differences up to $\Delta T = 134\,\mathrm{K}$. Note that the attainable temperature difference is higher in this configuration due to the different thermo-physical properties of the stack material (notably, we evaluated the thermal conductivity of the ceramics stack to be an order of magnitude greater than that of the stacked wiremesh). These results show a behavior very similar to the expected one [see Fig. 4(c)], with the amplitude ratio of incident waves varying gradually from 1 : 1 to a 16.2 : 1 while the relative phase shifts from 18° to −52°. (The gray line is a visual guide to improve readability.)

Each data point in Fig. 5(a) is then used as an excitation condition for the two-port, which should then act as a coherent perfect absorber, with minimal outgoing waves. Fig. 5(b) reports the amplitudes of the wave exiting the system, normalized such that the amplitude of excitation is unitary $\sum |p_{in}|^2 = 1$.

From the measurement of the amplitudes of incident $p^{\pm}_{in}$ and outgoing $p^{\pm}_{out}$ waves, the absorption coefficient α of the system is expressed:

$$\alpha = 1 - \frac{|p^{+}_{out}|^2 + |p^{-}_{out}|^2}{|p^{+}_{in}|^2 + |p^{-}_{in}|^2}. \tag{11}$$

The experimental absorption coefficient of the coherent perfect absorber is presented in Fig. 5(c) with square markers, and it is larger than 99.9 % for most of the temperature range and close to the expected value of $\alpha_{th} = 1 - \lambda^2_{min}$, shown with round markers.

Fig. 6 presents observations of the behavior of the system in the time domain. observations of the behavior of the system in the time domain. Though no temporal measurements were made, reconstructed data are presented based on the measurements of the scattering matrix of the system and the deduction of its eigenvalues/vectors. On the basis of the highest temperature difference measured previously $\Delta T = 136$, the top figures 6(a-b) present the normalized incident waves exciting the system from either side with relative amplitudes and phase given by the eigenvectors reported in Fig. 5(a). The lower figures 6(c-d) present, with the same respective, the scattered components, i.e. the waves reflected and transmitted by the TAN. The amplitude and phase of this components are obtained from the measured scattering coefficients of the TAN. It appears clear how the specifically designed scatterer has reflection and transmission coefficients allowing, with the proper excitation defined by the eigenvectors of the system, outgoing components on each side to have the same amplitudes and opposite phases. The result of simultaneous excitation in these conditions, by application of the superposition principle shown by the green lines, is the cancellation the scattered components resulting in quasi-null outgoing wave amplitudes. As is to be expected, the reconstructed amplitudes $p^{+}_{out} \simeq 1 \times 10^{-3}$, $p^{+}_{out} \simeq 1.5 \times 10^{-2}$ are close to the experimental ones shown on Fig. 5(b) (resp. the yellow diamond at 4×10^{-3} and the yellow disk at 2×10^{-2}).

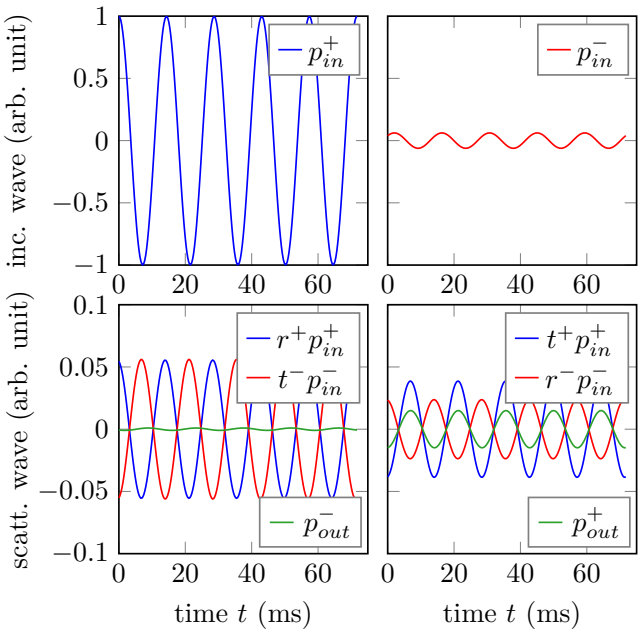


FIG. 6. Reconstructed time domain signals on either sides of the TAN in the case of the highest temperature in 5: $\Delta T = 134$, $f = 65.2$. (a)&(b) Incident waves respectively in the (x) and $(-x)$-directions, with relative amplitudes $|p^{-}_{in}|/|p^{+}_{in}| = 16.2$ and a phase difference $\angle(p^{-}_{in}/p^{+}_{in}) = 50.29$ (yellow triangle in Fig. 5(a)). (c)&(d) Scattered components of the wave, obtained from the scattering matrix of the TAN. Blue lines show the components deriving from the wave impinging in the (x)-direction, red lines show the components deriving from the wave impinging in the $(-x)$-direction. The green lines are the outcoming waves, sums of both scattered components on each side resulting from the simultaneous excitation.

VI. CONCLUSION

Experimental demonstration has been provided of the capability for thermoacoustic networks to create nonreciprocal acoustic systems with a high potential of tunability for various scattering properties. In particular, a system has been characterized which demonstrates asymmetric transmission of 18 dB, without reflections, and with balanced amplification/damping in opposite directions. A second demonstration has highlighted the possibility to make a coherent perfect absorber, that keeps the nonreciprocal properties inherent to thermoacoustic systems. The system has been shown to keep its absorption properties over a large span of temperature differences, allowing its effectiveness for largely disparate conditions of excitation. All of these behaviors can be modeled and predicted by the well-established linear theory of thermoacoustics, requiring only a good geometrical characterization of the unit cell.

Beyond the design choices made in this study, thermoacoustics offers several possibilities to generate systems exhibiting single frequency, as well as broadband

behaviors where exotic nonreciprocal scattering can be achieved. We believe this experimental study, as a proof of concept, may open the route to new interests in using thermoacoustics as a mean to generate tunable nonreciprocal systems.

ACKNOWLEDGMENTS

The authors wish to thank Y. Auregan and V. Pagneux for their remarks and suggestions about this work.

This work is supported by the French National Agency for Research (SelfiXs Project No. ANR-18-CE92-0001).

AUTHOR DECLARATION

The authors have no conflicts to disclose.

DATA AVAILABILITY STATEMENT

The data that support the findings of this study are available within the article.

[1]Z. Zhang, P. Delplace, and R. Fleury, "Superior robustness of anomalous non-reciprocal topological edge states," Nature **598**, 293–297 (2021).
[2]B.-I. Popa and S. A. Cummer, "Non-reciprocal and highly nonlinear active acoustic metamaterials," Nat. Commun. **5** (2014), 10.1038/ncomms4398.
[3]T. Devaux, V. Tournat, O. Richoux, and V. Pagneux, "Asymmetric acoustic propagation of wave packets via the self-demodulation effect," Phys. Rev. Lett. **115** (2015), 10.1103/physrevlett.115.234301.
[4]R. Fleury, D. L. Sounas, C. F. Sieck, M. R. Haberman, and A. Alu, "Sound isolation and giant linear nonreciprocity in a compact acoustic circulator," Science **343**, 516–519 (2014).
[5]M. Naghdi and F. Farzbod, "Acoustic nonreciprocity in coriolis mean flow systems," J. Acoust. Soc. Am. **143**, 230–236 (2018).
[6]C. Saverna, Y. Aurégan, and V. Pagneux, "Non-reciprocal scattering in shear flow," J. Acoust. Soc. Am. **146**, 1051–1060 (2019).
[7]R. Fleury, D. L. Sounas, and A. Alù, "Subwavelength ultrasonic circulator based on spatiotemporal modulation," Physical Review B **91**, 174306 (2015).
[8]C. F. Sieck, A. Alù, and M. R. Haberman, "Origins of willis coupling and acoustic bianisotropy in acoustic metamaterials through source-driven homogenization," Phys. Rev. B **96**, 104303 (2017).
[9]N. Geib, A. Sasmal, Z. Wang, Y. Zhai, B.-I. Popa, and K. Grosh, "Tunable nonlocal purely active nonreciprocal acoustic media," Physical Review B **103**, 165427 (2021).
[10]G. Penelet, V. Pagneux, G. Poignand, C. Olivier, and Y. Aurégan, "Broadband nonreciprocal acoustic scattering using a loudspeaker with asymmetric feedback," Physical Review Applied **16**, 064012 (2021).
[11]H. Nassar, B. Yousefzadeh, R. Fleury, M. Ruzzene, A. Alù, C. Daraio, A. N. Norris, G. Huang, and M. R. Haberman, "Nonreciprocity in acoustic and elastic materials," Nat. Rev. Mater. **5**, 667–6 85 (2020).
[12]C. Rasmussen, L. Quan, and A. Alù, "Acoustic nonreciprocity," J. Appl. Phys. **129**, 210903 (2021).
[13]G. W. Swift, "Thermoacoustic engines," J. Acoust. Soc. Am. **84**, 1145–1180 (1988).
[14]T. Jin, J. Huang, Y. Feng, R. Yang, K. Tang, and R. Radebaugh, "Thermoacoustic prime movers and refrigerators: Thermally powered engines without moving components," Energy **93**, 828–853 (2015).
[15]G. Chen, L. Tang, B. Mace, and Z. Yu, "Multi-physics coupling in thermoacoustic devices: A review," Renewable Sustainable Energy Rev. **146**, 111170 (2021).
[16]T. Biwa, H. Nakamura, and H. Hyodo, "Experimental demonstration of a thermoacoustic diode," Phys. Rev. Appl **5** (2016), 10.1103/physrevapplied.5.064012.
[17]G. Poignand, C. Olivier, and G. Penelet, "Parity-time symmetric system based on the thermoacoustic effect," J. Acoust. Soc. Am. **149**, 1913–1922 (2021).
[18]H. Hao and F. Semperlotti, "Band structure and effective properties of one-dimensional thermoacoustic bloch waves," Phys. Rev. B **104**, 104303 (2021).
[19]C. Olivier, G. Poignand, M. Malléjac, V. Romero-García, G. Penelet, A. Merkel, D. Torrent, J. Li, J. Christensen, and J.-P. Groby, "Nonreciprocal and even Willis couplings in periodic thermoacoustic amplifiers," Phys. Rev. B **104**, 184109 (2021).
[20]Y. D. Chong, L. Ge, H. Cao, and A. D. Stone, "Coherent perfect absorbers: Time-reversed lasers," Phys. Rev. Lett. **105** (2010), 10.1103/physrevlett.105.053901.
[21]J. Z. Song, P. Bai, Z. H. Hang, and Y. Lai, "Acoustic coherent perfect absorbers," New J. Phys. **16**, 033026 (2014).
[22]G. W. Swift, *Thermoacoustics: a unifying perspective for some engines and refrigerators* (Acoustical Society of America, 2002).
[23]N. Rott, "Damped and thermally driven acoustic oscillations in wide and narrow tubes," Z. Angew. Math. Phys. **20**, 230–243 (1969).
[24]W. P. Arnott, H. E. Bass, and R. Raspet, "General formulation of thermoacoustics for stacks having arbitrarily shaped pore cross sections," J. Acoust. Soc. Am. **90**, 3228–3237 (1991).
[25]M. R. Stinson and Y. Champoux, "Propagation of sound and the assignment of shape factors in model porous materials having simple pore geometries," J. Acoust. Soc. Am. **91**, 685–695 (1992).
[26]G. Penelet, S. Job, V. Gusev, P. Lotton, and M. Bruneau, "Dependence of sound amplification on temperature distribution in annular thermoacoustic engines," Acta Acust. united Ac. **91**, 567–577 (2005).
[27]M. L. Munjal and A. G. Doige, "Theory of a two source-location method for direct experimental evaluation of the four-pole parameters of an aeroacoustic element," J. Sound Vib. **141**, 323–333 (1990).
[28]H. Bodén and M. Åbom, "Influence of errors on the two-microphone method for measuring acoustic properties in ducts," J. Acoust. Soc. Am. **79**, 541–549 (1986).
[29]J.-P. Dalmont, J. Kergomard, and X. Meynial, "Réalisation d'une terminaison anéchoïque pour un tuyau sonore aux basses fréquences," C. R. Acad. Sci. Paris **309**, 453–458 (1989).
[30]F. Fohr and E. Portier, (2019).
[31]Y. Aurégan and R. Starobinski, "Determination of acoustical energy dissipation/production potentiality from the acoustical transfer functions of a multiport," Acta Acustica united with Acustica **85**, 788–792 (1999).
[32]M. Farhat, W. W. Ahmad, A. Khelif, K. N. Salama, and Y. Wu, "Enhanced acoustic pressure sensors based on coherent perfect absorber-laser effect," J. Appl. Phys. **129**, 104902 (2021).
[33]Z. Gu, T. Liu, H. Gao, S. Liang, S. An, and J. Zhu, "Acoustic coherent perfect absorber and laser modes via the non-hermitian dopant in the zero index metamaterials," J. Appl. Phys. **129**, 234901 (2021).